Barenji, AB, Russo, MB, Jabar, S, Kotadia, HR, Ceglarek, D, Ayarkwa, KF, Smith, JR and Franciosa, P

Effect of cooling rate on metallurgical and mechanical properties in continuous wave laser welding of hot-dip galvanised steel-to-aluminium sheets in a zero part-to-part gap lap joint configuration

Journal of Advanced Joining Processes 11 (2025) 100290

Contents lists available at ScienceDirect

Journal of Advanced Joining Processes

journal homepage: www.sciencedirect.com/journal/journal-of-advanced-joining-processes

Effect of cooling rate on metallurgical and mechanical properties in continuous wave laser welding of hot-dip galvanised steel-to-aluminium sheets in a zero part-to-part gap lap joint configuration

A. Baghbani Barenji [a,*], M.B. Russo [b], S. Jabar [a], H.R. Kotadia [c], D. Ceglarek [a], K.F. Ayarkwa [d], J.R. Smith [d], P. Franciosa [a]

[a] WMG, The University of Warwick, Coventry, CV4 7AL, UK
[b] Department of Engineering, University of Campania Luigi Vanvitelli, Aversa, 81031, Italy
[c] School of Engineering, Liverpool John Moores University, Liverpool, L3 3AF, UK
[d] Jaguar Land Rover Limited, Abbey Road, Whitley, Coventry, CV3 4LF, UK

ARTICLE INFO

Keywords:
CW laser beam welding
Dissimilar Zn-coated steel to aluminium
Zn vaporisation
Intermetallic compounds
Cooling
Mechanical properties
Beam oscillation

ABSTRACT

Using a continuous wave (CW) laser with beam oscillation, this study elucidates the impact of passive and active cooling on welding hot-dip galvanised steel-to-aluminium sheets. The work investigates how cooling affects the formation of intermetallic compounds (IMCs) and the behaviour of Zn vapours, both of which are critical factors to the joint strength. IMCs are recognised as the most decisive factor in welding steel to aluminium, while Zn vapours significantly impact welding in a zero part-to-part gap overlap configuration. A 3D finite element method thermal model was employed to correlate the thermal cycles to the metallurgical and mechanical properties. The cooling rate without beam oscillation increased by 34% switching from passive to active cooling, while it was only 2.5% with oscillation present (2.5 mm lateral oscillation). Results revealed that active cooling influences Zn vapours and IMCs differently; faster cooling reduced total IMCs and Fe_2Al_5 phase and increased joint strength; however, it exacerbated spattering and weld discontinuity due to insufficient time for outgassing the Zn vapours from the molten pool. This adverse effect was more pronounced with beam oscillation due to larger molten pool. The experimental work also showed that despite beam oscillation does enlarge the connection area, the average shear stress was relatively lower compared to the case without oscillation, attributed to the increased thickness of the IMCs. Active cooling with water flow at 10 °C achieved 60% joint efficiency compared to parent aluminium, while beam oscillation reduced this to 54% but with half the strength variation. This highlights the complex, non-linear interplay between IMC formation, Zn vapour outgassing, and the dynamics of the molten pool.

Introduction

The mandate for net-zero emissions in the automotive industry demands the development and validation of novel products and processes to reduce CO_2 and greenhouse gas emissions (Hertwich et al., 2019). An effective strategy is the lightweighting of automotive bodies, where minimising vehicle weight while maintaining/maximising mechanical properties has been at the heart of research and industrial development for decades. The use of dissimilar materials in the automotive body is regarded as the way forward by many automakers, due to their potential to offer tailored properties (Yang et al., 2024). A notable example is the joining of steel and aluminium, a combination that has garnered substantial interest from both research and industry (Wallerstein et al., 2021). This pair leverages complementary properties, such as the high strength and weldability of steel with the high strength-to-weight nature of the aluminium (Shah and Ishak, 2014).

Acknowledging parallel research endeavours related to corrosion protection and end-of-life recycling (Karim and Park, 2020), this paper addresses the metallurgical and mechanical problem posed by formation of brittle and low-toughness phases known as intermetallic compounds (IMCs) (Kotadia et al., 2022; Jabar et al., 2023), and the interplay with Zn vapours. The formation and growth of IMCs are driven by diffusion

* Corresponding author.
E-mail address: Ali.Baghbani-Barenji@warwick.ac.uk (A.B. Barenji).

https://doi.org/10.1016/j.jajp.2025.100290

Available online 31 January 2025

mechanisms, with peak temperature and diffusion time being critical parameters (Singh et al., 2019; Xia et al., 2019). Controlling these parameters demands a low-heat input process with fast solidification. Laser beam welding is a highly suitable process for this purpose, as already demonstrated in recent years (Kuryntsev, 2021; Quazi et al., 2020; Ma et al., 2023). Notably, pulsed lasers have been used to induce fast thermal cycles (below the μs time characteristic) to reduce the formation of IMCs. Despite the research has shown remarkable mechanical properties (Chludzinski et al., 2021), pulsed lasers are currently only available in the low power range below 1 kW for thin sheets (< 1 mm thickness). For thick sheets continuous wave (CW) lasers have displaced that.

In addition to diffusion time and peak temperature, controlling the cooling rate is a common and efficient way for mitigating IMCs (Casalino et al., 2017; Borrisutthekul et al., 2007). Faster cooling can decrease both diffusion time and peak temperature and improve the mechanical strength (Borrisutthekul et al., 2007). An interesting proposition is the integration of an external cooling system with a CW laser welding process. For example, backing block materials can promote fast heat dissipation, hence obtaining high cooling rates (Borrisutthekul et al., 2007; Pardal et al., 2014; Liedl et al., 2011). Backing blocks are made of metals with high thermal diffusivity, such as copper, and extract the applied heat through fast conduction. Borrisutthekul et al. (2007) utilised three different backing blocks made of titanium (thermal conductivity = 16.7 W/m·k), steel (thermal conductivity = 44 W/m·k) and copper (thermal conductivity = 394 W/m·k) and showed the negative correlation between the thermal conductivity (directly proportional to thermal diffusivity) of the backing block and the IMCs thickness. This was explained by the fact that as thermal conductivity increases, heat sinking grows and the time in which weld pool is molten becomes shorter and as a result diffusion of Fe and Al atoms decreases. Superiority of copper backing block was reported in other works as well. For example, laser spot joining of dissimilar steel to aluminium was carried out, comparing the effects of aluminium and copper backing blocks, and the superior influence of copper backing block in reducing the thickness of IMCs was illustrated in Pardal et al. (2014). Similarly, Liedl et al. (2011) checked copper and aluminium backing block materials in laser welding of steel to aluminium. They achieved the highest strength using copper backing block in all the applied energy ranges.

It should be noted that although fast cooling in dissimilar welding can help mitigate the formation of IMCs, it does not always lead to improved mechanical strength. The effect of fast cooling on the mechanical properties of dissimilar welds depends on several factors, such as the cooling rate's influence on the microstructure, the materials being welded, and the specific welding process. For instance, rapid cooling can induce microstructural changes that may result in the formation of martensite in certain steels. Martensite is a hard phase that is susceptible to solidification cracks and reduced ductility, which can compromise the overall mechanical performance (Zarei et al., 2024). Moreover, fast cooling typically increases residual stresses (Xie et al., 2022), which further underscores the importance of finding an optimal cooling rate for each specific application. The differing thermal conductivities of the materials being welded can also lead to unequal temperature distributions and cooling rates across the weld. For example, joining carbon steel AISI 1060 with austenitic stainless steels AISI 304 and 420 can produce distinct cooling behaviours due to their different thermal properties (Zarei et al., 2024). This difference in thermal conductivities can result in challenges related to controlling the weld's microstructure and, consequently, the weld's mechanical properties.

Nevertheless, IMCs are not the only difficulty and the presence of a protective Zn coating on the steel surface is another obstacle complicating the joining of a Zn-coated steel in a zero-gap overlap configuration (Kashani et al., 2015). Comprehending the influence of the Zn coating is essential due to its significance in industrial needs - Zn coating is widely utilised as corrosion protection for steel sheets, especially in automotive body construction. Since Zn coating evaporates during welding due to its low vaporisation temperature (approx. 907 °C), in an overlap welding configuration the Zn vapours can lead to two types of problems. First, Zn vapours have tendency to shield the processed area and induce unwanted laser beam reflections, ultimately leading to a non-uniform interaction between the laser beam and the material (Dasgupta et al., 2007; Allen et al., 2020). Second, Zn vapour can become entrapped in the weld pool, causing defects such as spatter, pores, and lack of fusion (Chen et al., 2010). This has been reported in various studies on similar laser welding Zn-coated steels (Hao et al., 2022). However, only a few studies on dissimilar laser welding Zn-coated steel to aluminium (Ma et al., 2014) have addressing this issue. The current practice is to use dimples produced via a fast-moving laser beam (Ozkat et al., 2017). In essence, the dimples work as a spacer between the two sheets in lap joint and let the Zn vapour escape during the welding process. Although this is the industry best practice, it adds significant complexity and increase cycle time, necessitating parallel stations, hence escalating costs.

While the effect of cooling rate on IMCs has been investigated in a vast range of studies, very limited research with scattered results is currently available to elucidate the effect of cooling rate in laser weldments of Zn-coated steel to aluminium, with impact on both IMCs and Zn vaporisation. This paper aims to address this gap and will study the impact of passive and active cooling on welded Zn-coated DC01 mild steel to 5251-H22 aluminium sheets in a zero part-to-part gap overlap configuration. Microstructural observations, mechanical testing, and chemical characterisation were performed to find the interconnection between IMCs thickness, Zn vaporisation and joint strength. A 3D finite element method (FEM) model was also developed to predict the thermal cycles at the weld interface and correlate them to the metallurgical and mechanical properties.

Experimental procedure

Materials

Laser beam welding trials were performed on DC01 mild steel and 5251-H22 aluminium, each with a thickness of 1.5 mm. The chemical composition, along with the maximum shear stress values, for each of the parent materials, are detailed in Table 1. Notably, the DC01 mild steel sheet is hot-dip galvanised, with a 10 μm layer of zinc on both sides. The steel and aluminium samples were both cut into rectangular coupons, each measuring 48 mm in width and 112 mm in length. To ensure that the surface of the coupons was free from any contaminants, each coupon was carefully cleaned by wiping it with acetone. The Zn coating on the steel and the oxide layer on the aluminium were not removed.

Laser welding procedure

The laser welding trials were carried out using an adjustable ring-mode (ARM) Coherent CW fibre (Coherent ARM FL 10,000) laser system that has a maximum combined power output of 10 kW (with maximum 5 kW for both core and ring beam). A WeldMaster YW52 Scan&Track remote welding head, (Precitec GmbH) capable of oscillating the laser beam, was utilised to deliver the laser energy to the workpiece. The full technical specifications and details of the laser system are provided in Table 2.

Table 1
Chemical compositions (wt. %) and shear stress of the DC01 mild steel and 5251-H22 aluminium alloy.

DC01 Steel	Fe	C	Mn	P	S	Shear stress (MPa)
	Bal.	<0.12	<0.6	<0.045	<0.045	150–230
5251-H22 Aluminium	Al	Mg	Fe	Mn	Si	Shear stress (MPa)
	Bal.	1.7–2.4	<0.5	0.1–0.5	<0.4	110–160

Table 2
Details of the laser welding system.

Parameter	Units	Core	Ring
Maximum power	W	5000	5000
Optical fiber diameter	μm	100	290
Spot diameter on focus, d_0	μm	200	580
Collimating length	mm	150	
Focusing length	mm	300	
Rayleigh length, Z_R	mm	2.57	6.25
Nominal central wavelength	nm	1070	

The welding head was mounted on a 6-axis ABB robot system and inclined at 5° around the Y axes (negative direction) to protect the optical system from possible damages by reflected light. The laser beam was focussed on the top surface of the sample. The focal offset, A_z, is defined as the distance along the beam between the laser beam focal point and the material surface. Hence, when the focal point is on the top surface, A_z value is zero. No filler wire nor shielding gas was utilised in the welding trials. Fig. 1 shows the welding setup. The functionality of the copper cooling system was twofold: (1) to control the cooling rate of the bottom surface of the aluminium sample (via the copper plate - item 7 in Fig. 1(b)) and the top surface of the steel sample (via the top copper bar - item 8 in Fig. 1(b), 2) to clamp the specimen to a zero part-to-part configuration. Controlling the cooling rate was enabled by water flowing through 12 channels (8 mm diameter) machined in the copper plate and also 4 channels (8 mm diameter) in the top copper bar. Copper was chosen due to the high thermal diffusivity (1.17e2 mm^2/s at room temperature (Daurelio et al., 1986)). The channels were then fitted with connectors and hosed to an SMC HRSE012/018/024 series chiller (item 3 in Fig. 1(a)) delivering 6 l/min DI water. N-type thermocouples with a Sefram DAS220 digital data logger were used to monitor the water temperature at the inlet/outlet of the channels.

Design of experiments

Welding trials were performed in a nominal zero part-to-part gap overlap configuration with steel on top.

Welding parameters were divided in two groups: group "a" – no beam oscillation with large beam defocus (A_z = 12 mm) and welding speed of 80 mm/s; group "b" – with beam oscillation, no beam defocus and welding speed of 40 mm/s. For each group 4 sub-cases were tested: room temperature (RT at 25 °C) and no water flow (*passive cooling*), and then constant water flow at 6 l/min for 3 water temperatures of 25 °C, 17 °C and 10 °C (*active cooling*); water temperature below 10 °C was avoided due to the risk of condensation on the water pipes and the copper cooling system. Power and speed were adjusted for group "a" and "b" to achieve an average weld penetration depth in the range 300–400 μm; this was motivated by the need to avoid the excessive mixing of steel and aluminium as already presented in similar investigations (Jabar et al., 2023). The proposed design of experiments allowed to analyse the effect of passive and active cooling in group "a" with a non-oscillating beam moving linearly in X; as well as introduce the additional effect of lateral beam oscillation in group "b". In order to compare the energy inputs between the two groups, the volumetric energy of the laser beam was calculated as in Eq. (1) (Guo et al., 2019), where A_s is the spot area at the A_z value and defined in Eq. (2) (Sun et al., 2021), with d_0 and Z_R the average spot diameter on focus and Rayleigh length (see Table 2), respectively. In Eq. (3) (Sun et al., 2021) S_a is the maximum magnitude of the beam velocity that accounts for the later motion in the Y direction during oscillation.

$$Q = \frac{P}{S_a \cdot A_s} \left[\frac{J}{mm^3}\right] \tag{1}$$

$$A_s = \pi \frac{d_s^2}{4} \left[mm^2\right], \; d_s = d_0 \sqrt{1 + \left(\frac{A_z}{Z_R}\right)^2} \left[mm\right] \tag{2}$$

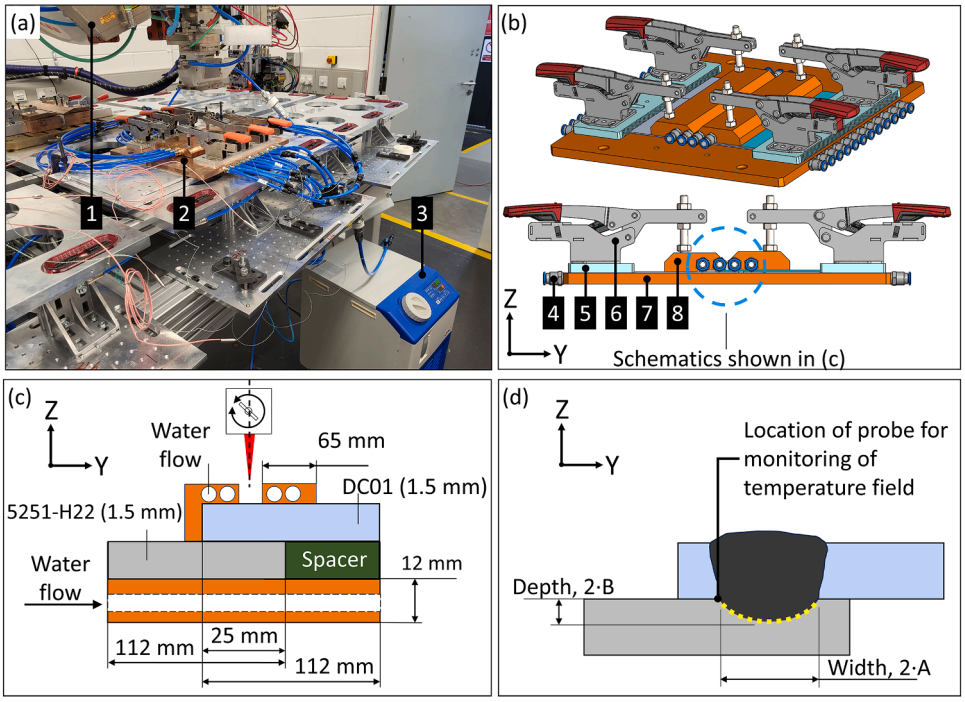

1 - Welding head. 2 - Copper cooling system. 3 - Chiller. 4 - Water connectors. 5 - Mounting plate clamps. 6 - Toggle clamp. 7 - Copper plate with water flow in Y. 8 - Top copper bar with water flow in X.

Fig. 1. (a) Welding setup; (b) mechanical design of the copper cooling system with clamps; (c) schematics of the welding setup with the cooling system; (d) schematics of joint width, depth, and connection area (yellow dashed line) on the aluminium interface.

$$S_a = \sqrt{S^2 + S_y^2},\ S_y = 2\pi f \cdot A_y \left[\frac{mm}{s}\right] \quad (3)$$

Each weld sample was repeated four times: three for lap shear tensile testing and one for microstructural analysis and chemical characterisation.

Weld characterisation and testing

Following the welding trials, specimens for characterisation analysis were extracted from three locations along the weld length: one sample in the middle of the weld and two samples positioned 10 mm away from the start and end of the weld. These samples were then mounted in conductive Bakelite resin for further preparation. The specimens underwent a grinding process using 1000 sandpaper, followed by a polishing stage with 9 μm and 3 μm solutions and 0.06 μm silica slurry to obtain a very fine surface.

Initial microstructural observations from the top surface (steel) and interface (aluminium) were conducted using a Keyence VHX7000 optical microscope to observe the weld seam and connection area, respectively. Then higher magnifications using a scanning electron microscope (SEM) Zeiss Sigma was acquired to investigate the IMCs. The advantages of ImageJ software were taken to quantify the area and thickness of IMCs, and penetration width, depth, and connection area.

Energy-dispersive X-ray spectroscopy (EDS) was used for the analysing Fe and Al mixing through low magnification chemical mapping. The analysing condition was a 20 kV accelerating voltage, a 16 nA current and up to 300,000 cps input count plus a dwell time of 250 ms. To determine the elemental composition of specific regions (IMCs or base material) 5 EDS spot analysis were taken from each marked region and the resulting spectrum was employed to identify the elements present, and their concentrations using Aztec software. By correlating the resulted elemental composition to potential phases in the Fe-Al phase diagram and comparing with previous literature, the phases in the material can be inferred.

Lap shear tensile tests were performed in accordance with the EN ISO 14273 standard (EN ISO, 2000) on rectangular laser welded specimens using an Instron 30 kN tensile machine at 2 mm/min tension rate. Shear stress was measured using the Eq. 4, where F [N] is the maximum load at fracture and CA [mm^2] is the connection area at the interface. Since the weld fracture always happened at the interface of the joint, CA, was obtained by fitting an arc of ellipse (Barnard et al., 2001), whose semi-axis are A and B (Fig. 1(d)) and calculating one half lateral area of the elliptical cylinder with height L (weld length).

$$Shear\ stress = \frac{F}{CA}\left[\frac{N}{mm^2}\right] \quad (4a)$$

$$CA = \frac{\pi\sqrt{2\left(A^2 + B^2\right)}\cdot L}{2}\left[mm^2\right] \quad (4b)$$

The Pearson's correlation was utilised to examine the correlation between the key parameters in this study. Further, ANOVA test was run with the acceptance level of 10 % to test the statistical significance of the outputs.

Numerical FEM model to predict thermal cycles

The thermal cycles during solidification were calculated using a 3D FEM transient model with heat conduction and phase change. The main assumptions of the model were: (1) irradiance is neglected; (2) phase change is modelled using the apparent heat capacity method (Artinov et al., 2018); (3) the laser absorbance is modelled via a scaling coefficient of the input laser power, as also proposed in previous studies (Dourado da Silva et al., 2023).

The dimensions of the simulated zone were 12 × 12 × 3 mm^3 (Fig. 2 (a)) ensuring the model reaches a steady state regime. The boundary conditions of the computational domain were set with natural convective heat flux between the sheets and the air - heat transfer coefficient in air, h_{air}, was assumed equal to 15 W/(m^2·K) at ambient temperature.

The heat sinking effect of the copper cooling system was modelled as in Eq. (5): in case of passive cooling, an "artificial" convective heat flux was introduced, where T_{amb} is the ambient temperature at 25 °C, and A_{ch} the surface area of the cooling channels; in case of active cooling, the temperature was set constant to the water temperature, T_{water}, as specified in Table 3. This assumption was deemed reasonable since the readings from the N-type thermocouples, at the inlet/outlet of the cooling channels, revealed only 1.0±0.3 °C variation in water temperature.

$$passive\ cooling \rightarrow h_{air}\cdot A_{ch}\cdot(T - T_{amb}) \quad (5a)$$

$$active\ cooling \rightarrow T = T_{water} \quad (5b)$$

A tetrahedral 3D mesh with linear elements (4 nodes per element) was generated. The computational domain was meshed with different resolutions of the weld and surrounding regions. The mesh was refined in regions experiencing higher temperature gradients, ensuring numerical accuracy, especially near the laser interaction zone (6 mm wide as shown in Fig. 2(a)). The coarse mesh size was 3 mm.

The thermal and physical properties of the steel and aluminium samples were generated from the JMATPRO® as depicted in Fig. 2(b), and assumed temperature-dependent.

The volumetric heat input, Q_{laser}, was modelled with a moving Gaussian-conical heat source, as specified in Eq. 6, where r_b (50 μm) and H_h (3 mm) are the radius of the cone and its height, respectively. The coefficient α was introduced to account for the laser absorbance (Simonds et al., 2018) and calibrated via experiments.

$$R = \frac{d_s}{2} - \frac{\left(r_b - \frac{d_s}{2}\right)}{H_h} z\ [mm] \quad (6a)$$

$$r = \sqrt{(x - x_s)^2 + (y - y_s)^2 + z^2}\ [mm] \quad (6b)$$

$$\begin{cases} x_s = S\cdot t \\ y_s = A_y cos(2\pi f t) \end{cases}\ [mm] \quad (6c)$$

$$Q_{laser}(x, y, z, t) = \frac{\alpha P}{\pi d_s^2 H_h}\exp\left(-2\frac{r^2}{R^2}\right)\left[\frac{W}{mm^3}\right] \quad (6d)$$

The time step for the simulation was set to 0.0005 s to capture rapid thermal changes due to laser heating. The simulation time, t, covered the duration of the welding process and post-weld cooling, extending twice the welding time to observe cooling behaviour. The laser switch-off time was 0.0375 s for group "a" and 0.025 s for group "b". The simulation began with an initial temperature of 25 °C for the entire computational domain.

The temperature field was then monitored for all the tested scenarios in Table 3 at the probe location shown in Fig. 1(d). For each time step, temperature and cooling rate were extrapolated. The FEM model was coded in the PDE toolbox of Matlab® 2024a and solved on a Z840 workstation. A mesh-independent solution was achieved with a finer mesh size of 50 μm in the laser interaction zone, approximating 200,000 elements in the computational domain.

Results and discussion

Calibration of numerical model

For all the simulations the scaling coefficient α was varied and the optimised value was set constant to 0.7 for all the tested cases. Fig. 3 shows the results of the calibration for two representative cases, yielding well correlated simulations to the actual experimental values. This

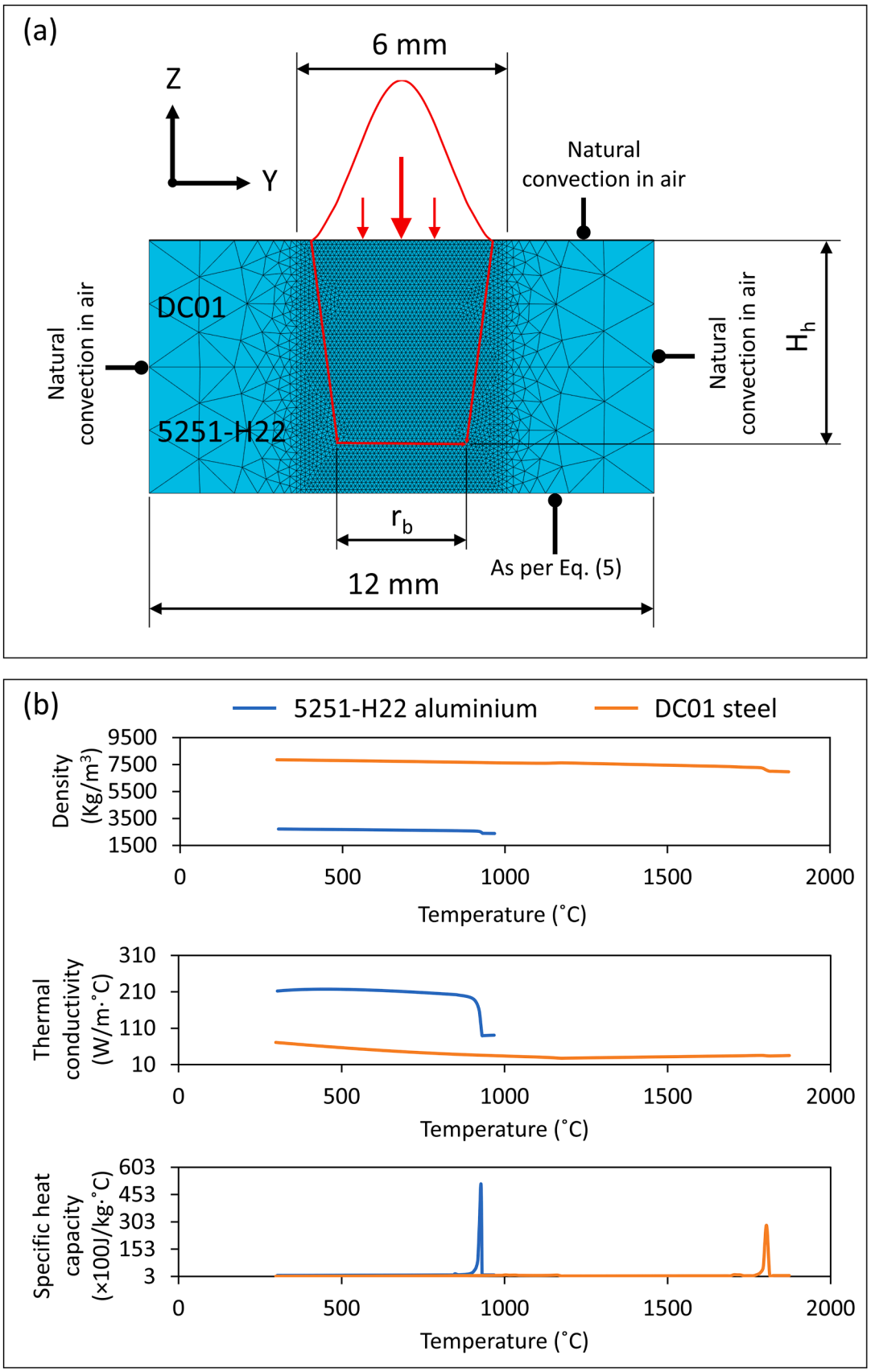

Fig. 2. (a) Details of the FEM model (heat source shown not in scale) with boundary conditions and heat source model. (b) Material properties imported from JMATPRO®.

Table 3
Parameters and processing conditions used in this study.

sample	group	Beam oscillation	Total power, P (W)	Speed, S (mm/s)	Focal offset, A_z (mm)	Total power density (MW/cm^2)	Volumetric energy, Q (J/mm^3)	Oscillation Frequency, f (Hz)	Oscillation amplitude, 2·A_y (mm)	Water Temperature, T_{water} (°C)
1	a	No	5850	80	12	1.05	81.74	-	0	RT no flow
2		No	5850	80	12	1.05	81.74	-	0	25
3		No	5850	80	12	1.05	81.74	-	0	17
4		No	5850	80	12	1.05	81.74	-	0	10
5	b	Yes	5500	40	0	10.50	23.68	100	2.5	RT no flow
6		Yes	5500	40	0	10.50	23.68	100	2.5	25
7		Yes	5500	40	0	10.50	23.68	100	2.5	17
8		Yes	5500	40	0	10.50	23.68	100	2.5	10

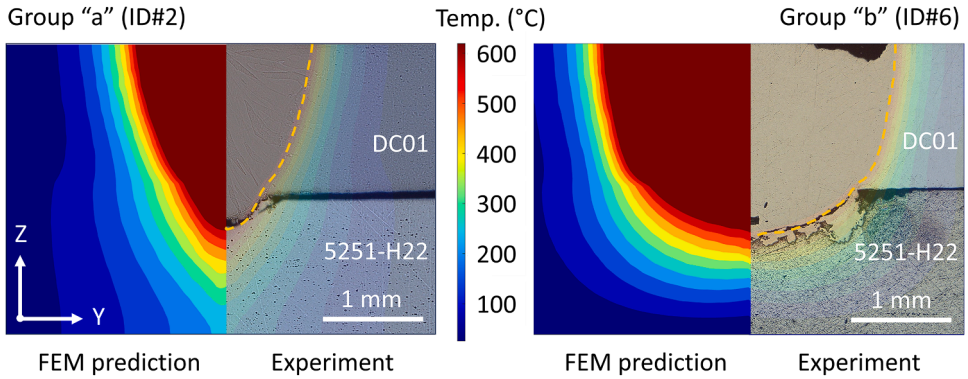

Fig. 3. Comparison of simulated and experimental cross-sectional data. The cross-section on the right-hand side is overlayed to the FEM prediction in partial transparency.

allows to confidently deploy the numerical model and provide useful insights about the temperature field, which are difficult to access via experiments due to technological difficulties.

Effect of the cooling rate

Fig. 4 shows the cross section of DC01 steel sheet (unwelded) and the elemental EDS map analysis showing the Fe and Zn content as well as thickness and distribution of the Zn coating on the surface. Fig. 5 (a, b) and (c, d) displays the temperature distribution and cooling rate for the samples welded in groups “a” (no oscillation) and group “b” (with oscillation) with magnified view of the highlighted regions below each section. These thermal values have been monitored at the interface between steel and aluminium as shown in Fig. 1 (d). The maximum values are synthetically reported in Table 4. Results suggest that, in general, active cooling reduces the peak temperature and increases the cooling rate. Lowering the water flow temperature (ID 2 to ID 4 and ID 6 to ID 8) further reduces the peak temperature and increases the cooling rate, although this effect is less significant compared to switching from passive (ID 1 and ID 5) to active cooling (ID 4 and ID 8).

Additionally, under the welding parameters used in this study, the peak temperature is slightly higher in group “b” samples (oscillation), and the cooling rate is also significantly higher in this group. The multiple thermal cycles observed in the group “b” samples (oscillation) are associated to multiple reheating/remelting of the weld pool. The maximum cooling rate changes drastically (34%) switching from passive (ID 1) to active (ID 2) cooling in group “a”; whereas, in samples with beam oscillation (group “b”), this change is only 2.5 % from ID 5 (passive cooling) to ID 6 (active cooling) at the same temperature.

The effect of the cooling process is discussed as follows:

- *reduction of the IMCs thickness*. The active cooling process with water flow in copper backing block provides additional cooling to the rapid solidification during the laser welding. Cooling impacts IMCs in two ways; first, it lowers the peak temperature, resulting in exponentially lower reaction rate according to Arrhenius relationship (Bouayad et al., 2003). This decreases the rate of IMCs formation. Second, faster cooling reduces the solidification time, and consequently, decreases the diffusion time, which reduces the interaction between Fe and Al atoms (less mixing). One example of reduction in IMCs thickness by increasing the cooling rate can be seen in Fig. 6, which compares the IMCs in two areas of sample ID 5 (Fig. 6 (b) and (c))

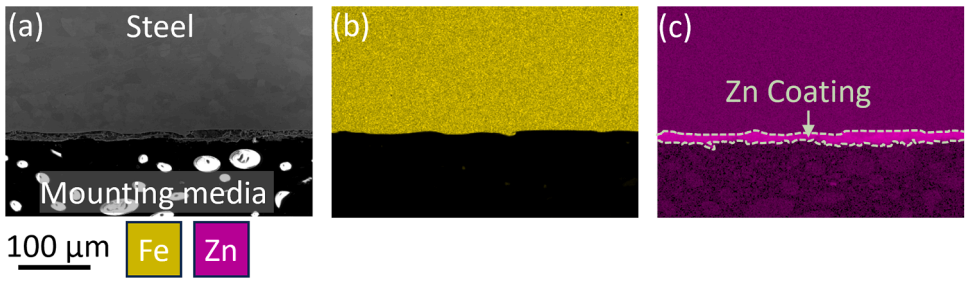

Fig. 4. (a) Cross-section of DC01 steel sheet, and EDS composition map analysis showing the (b) Fe content and (c) Zn distribution.

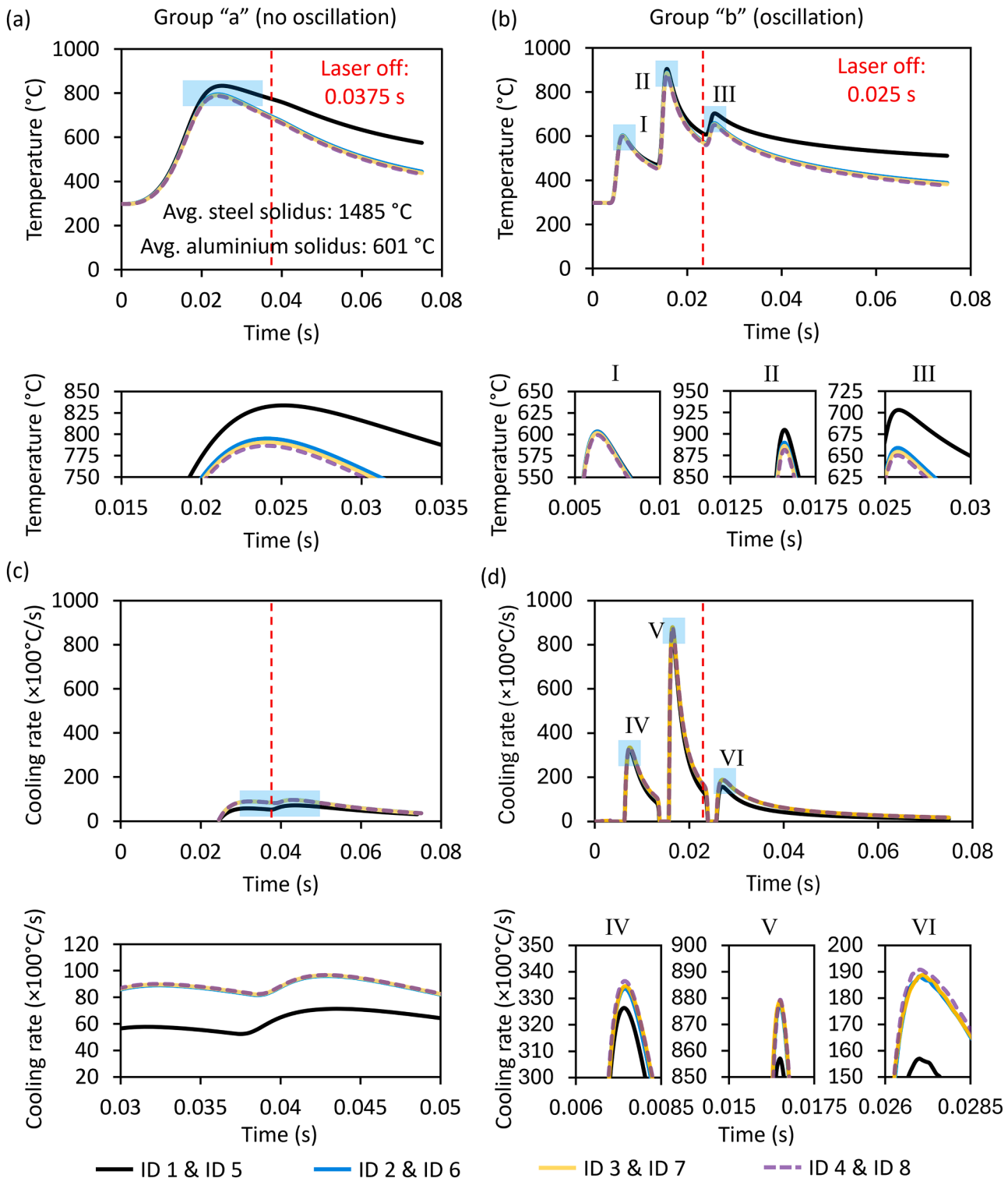

Fig. 5. (a) Temperature and (c) cooling rate diagrams for samples of group "a" (no oscillation); (b) temperature and (d) cooling rate diagrams for samples of group "b" (oscillation). The highlighted blue area is zoomed in below each diagram. The solidus temperature of steel and aluminium was taken from Anon (2025a, 2025b), respectively.

and in two areas of the sample ID 8 (Fig. 6 (d) and (e)). Fig. 6(a) sketches the location of the selected two areas and the method for measuring the total IMCs and Fe_2Al_5 phase. A decrease in Fe_2Al_5 and needle like Fe_4Al_{13} IMCs can be seen when 10 °C water flow is used. Fe_2Al_5 is known as the most brittle IMC in Fe-Al system. Therefore, it is more susceptible to cracking and fracture than other IMCs in this system like, $FeAl_3$ (or Fe_4Al_{13} at non-equilibrium condition), Fe_4Al_{13}, FeAl, $FeAl_2$, Fe_2Al_7 and Fe_3Al (Table 5) (Sadeghian and Iqbal, 2022). An instance of the typical fracture and cracking in or around the Fe_2Al_5 IMC can be observed in Fig. 6 (f).

Based on the Fe-Al phase diagram (Fig. 7) a range of IMCs can form depending on the ratio of Fe to Al. The development of specific intermetallic phases is influenced by factors such as welding time,

Table 4
Thermal properties obtained from Fig. 5.

Sample	Oscillation	Water Temperature (°C)	Peak temperature (°C)	Max. Cooling rate (°C/s)
ID 1	No	RT no flow	833.74	7141
ID 2	(group	25	794.84	9610
ID 3	"a")	17	790.53	9662
ID 4		10	786.66	9679
ID 5	Yes	RT no flow	904.89	85,709
ID 6	(group	25	889.56	87,781
ID 7	"b")	17	886.05	87,897
ID 8		10	881.62	87,935

temperature, and local composition (Xu et al., 2016). The properties of these IMCs are primarily determined by the differences in their crystal structure (Li et al., 2020), chemical bonding (Liu et al., 2017) and stoichiometry (Zhang et al., 2023). The type and quantity of IMCs significantly impact the mechanical properties due to variation in brittleness. Table 5 presents the crystal structure and microhardness values for different IMCs in the Fe-Al system. As solidification begins, the Fe_2Al_5 phase is initially formed (Eq. (7a)). The nucleation of Fe_2Al_5 occurs preferentially because it has a higher melting point (~ 1169 °C), and lower formation enthalpy and Gibbs free energy compared to $FeAl_3$ (Meng et al., 2020). The formation of a Fe_2Al_5 layer restricts the diffusion of Fe atoms from steel to Al. This results in a rapid decrease in Fe concentration at the interface of molten pool/Fe_2Al_5 layer, which in turn decreases the atomic ratio of Fe/Al. As the temperature drops to the melting point of Fe_4Al_{13} (~ 1160 °C), if Fe concentration at the interface is sufficient a peritectic reaction (Eq. (7b)) between Fe_2Al_5 and the liquid Al occurs. Ultimately, a two-layer structure of IMCs including Fe_2Al_5 and Fe_4Al_{13} forms at the interface (Meng et al., 2020).

$$2Fe + 5Al \rightarrow Fe_2Al_5 \quad (7a)$$

$$2Fe_2Al_5 + 3Al \rightarrow Fe_4Al_{13} \quad (7b)$$

According to literature Fe_2Al_5 and Fe_4Al_{13} are the most observed IMCs in Fe-Al system (Shang et al., 2021). However, as it can be seen in Fig. 6, FeAl and $FeAl_2$ phases are also visible in some regions. These IMCs are relatively rare and form in great amounts only under specific conditions that enable adequate diffusion and ordering (Beygi et al., 2023).

- *Intensification of the Zn vaporisation*. This is responsible for spattering and joint discontinuity during the welding. Faster cooling promotes spattering because there is less time for degassing. The reduced

Table 5
Common types of IMCs in Fe-Al system and their properties (Sadeghian and Iqbal, 2022).

IMC type	Chrystal structure	Microhardness (HV)
Fe_3Al	Ordered BCC	250–350
FeAl	Ordered BCC	400–520
Fe_2Al_7	Complex BCC	650–680
$FeAl_2$	Complex rhombohedral	1000–1050
Fe_2Al_5	BCC orthorhombic	1000–1100
$FeAl_3$	Highly complex monoclinic BCC	820–980

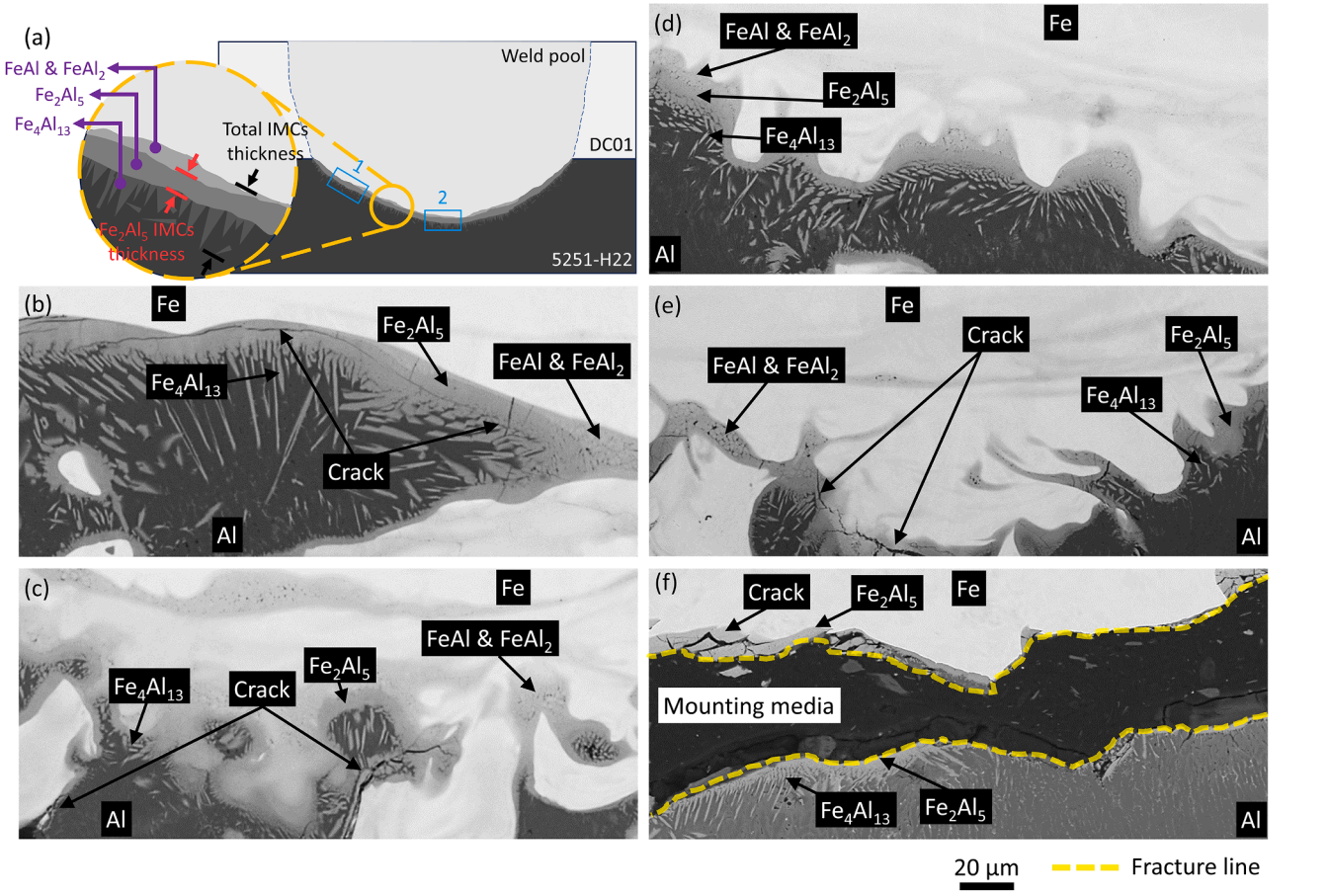

Fig. 6. (a) Schematic of weld cross-section indicating the two areas where micrographs were extracted, and the method for measuring the total and Fe_2Al_5 IMCs thickness. (b-c) Micrographs taken from areas 1 and 2, respectively in sample ID 5. (d-e) Micrographs taken from areas 1 and 2, respectively in sample ID 8. (f) Example of fracture happens in Fe_2Al_5 IMCs.

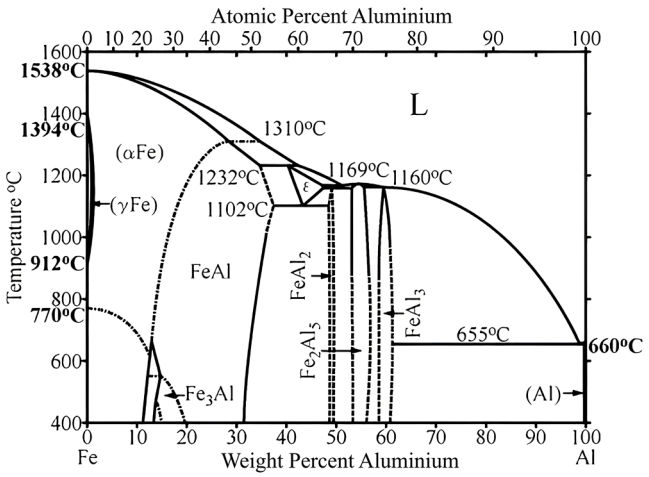

Fig. 7. Fe-Al binary phase diagram (Ozaki and Kutsuna, 2012).

solidification time traps more Zn vapours in the molten pool, leading to more spattering. This is in agreement with the findings in Singh et al. (2019), Daurelio et al. (1986). This observation is also proved by the EDS maps in Fig. 8, taken at the interface (aluminium) from sample ID 8.

Evolution of mechanical properties during welding

Fig. 9 links the main determining factors in this study, including lap shear stress, total and Fe_2Al_5 IMCs thickness, peak temperature, and cooling rate. Fig. 9(a) represents the lap shear stress results in group "a" (no oscillation) and group "b" (oscillation). It is observed that the application of water flow (active cooling) and enhancing the cooling rate (from ID 2 to ID 3 and ID 4) improves the strength compared to the passive cooling condition (ID 1), although improvement become marginal as water flow temperature decreases from ID 3 (17 °C) to ID 4 (10 °C). Similar behaviour can be seen when considering samples in group "b" (oscillation). Likewise, as active cooling is employed and water flow temperature decreases (from ID 6 to ID 7 and ID 8), strength growth is observed with negligible increase in ID 8. This improvement in strength with the increase of cooling rate is connected to the positive effect of faster cooling in reducing the IMCs thickness. A negative correlation of -0.90 and -0.85 is observed between the lap shear stress and total and Fe_2Al_5 IMCs thickness, respectively. The full correlation analysis can be found in Section "Impact of connection area and IMCs thickness on strength". Both faster cooling and faster welding reduces IMCs thickness in group "a" (no oscillation). Fig. 9 (b) and (c) displays the changes in total IMCs and Fe_2Al_5 IMC thickness, respectively. Once active cooling is applied, a decrease in total and Fe_2Al_5 IMCs thickness is observed (comparing ID 2 vs ID 1 and ID 5 vs ID 6 in Fig. 9 (b) and (c)). This trend continues as the water flow temperature decreases to 17 °C and 10 °C (ID 3 and ID 4 of group "a" (no oscillation), and ID 7 and ID 8 of group "b" (oscillation)). The changes are more pronounced in the samples with beam oscillation (Fig. 9 (b) and (c)). This is because more mixing is achieved in samples of group "b" (oscillation) due to slower welding speed and higher penetration depth compared to group "a". Furthermore, due to larger connection area (using beam oscillation) higher heat sinking is available in specimens of group "b" which is in accordance with the higher cooling rate in these samples compared to the samples of group "a" (Fig. 9(e)).

Comparing the changes in total and Fe_2Al_5 IMCs thickness with peak temperature and cooling rate (Fig. 9 (d) and 9 (e), respectively) signifies the positive effect of reduction in peak temperature and cooling rate enhancement (lower diffusion time) in declining the total and Fe_2Al_5 IMCs thickness. Changes in lap shear stress with increase in cooling rate is more evident in samples of group "b" (oscillation) where IMCs thickness also rapidly drop with cooling rate growth.

On average, samples of group "b" exhibit lower strength compared to group "a". This can be explained considering higher total and Fe_2Al_5 IMCs thickness in samples of group "b" according to Fig. 9 (b) and (c). It is apparent that increasing the joint area using beam oscillation in group "b" (oscillation) is not successful in increasing the strength. This is because IMCs thickness also grows as connection area and penetration depth enhances. Moreover, higher distortion and residual stress is expected with larger connection area. Another observation is the higher variation in shear stress in group "a". This cannot be justified only

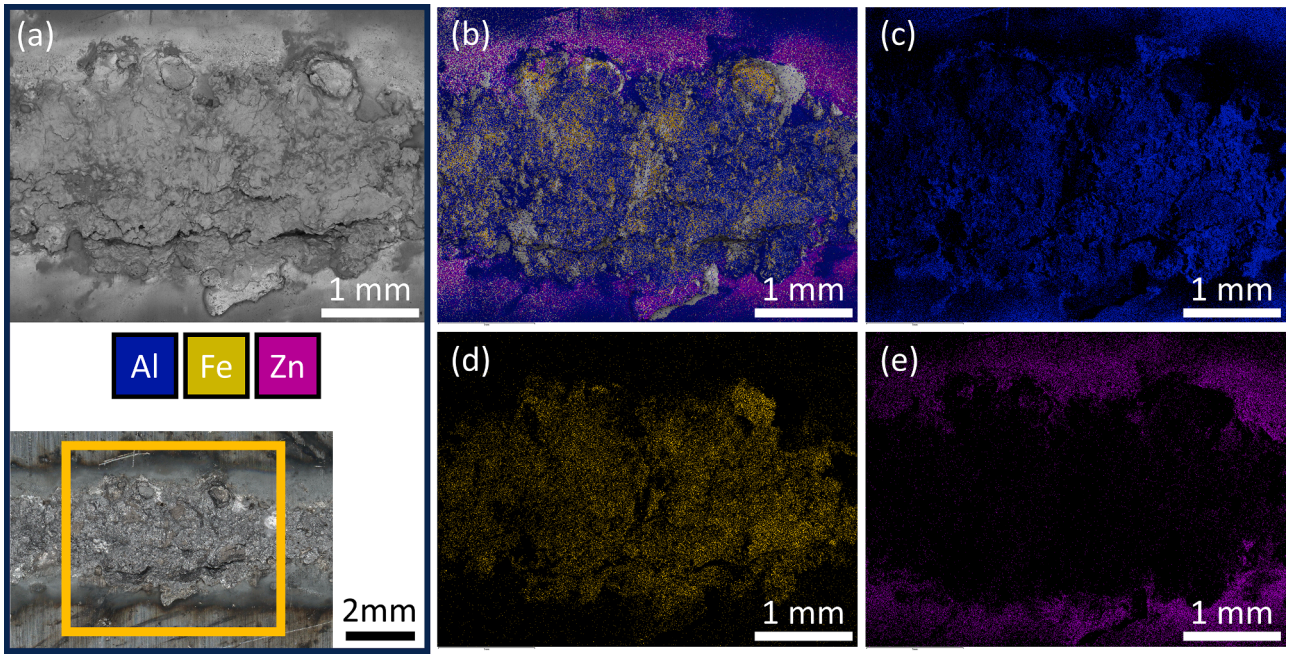

Fig. 8. (a) SEM and optical micrographs of the interface (aluminium) from ID 8 and the corresponding EDS map results for (b) all the elements, (c) Al, (d) Fe, and (e) Zn.

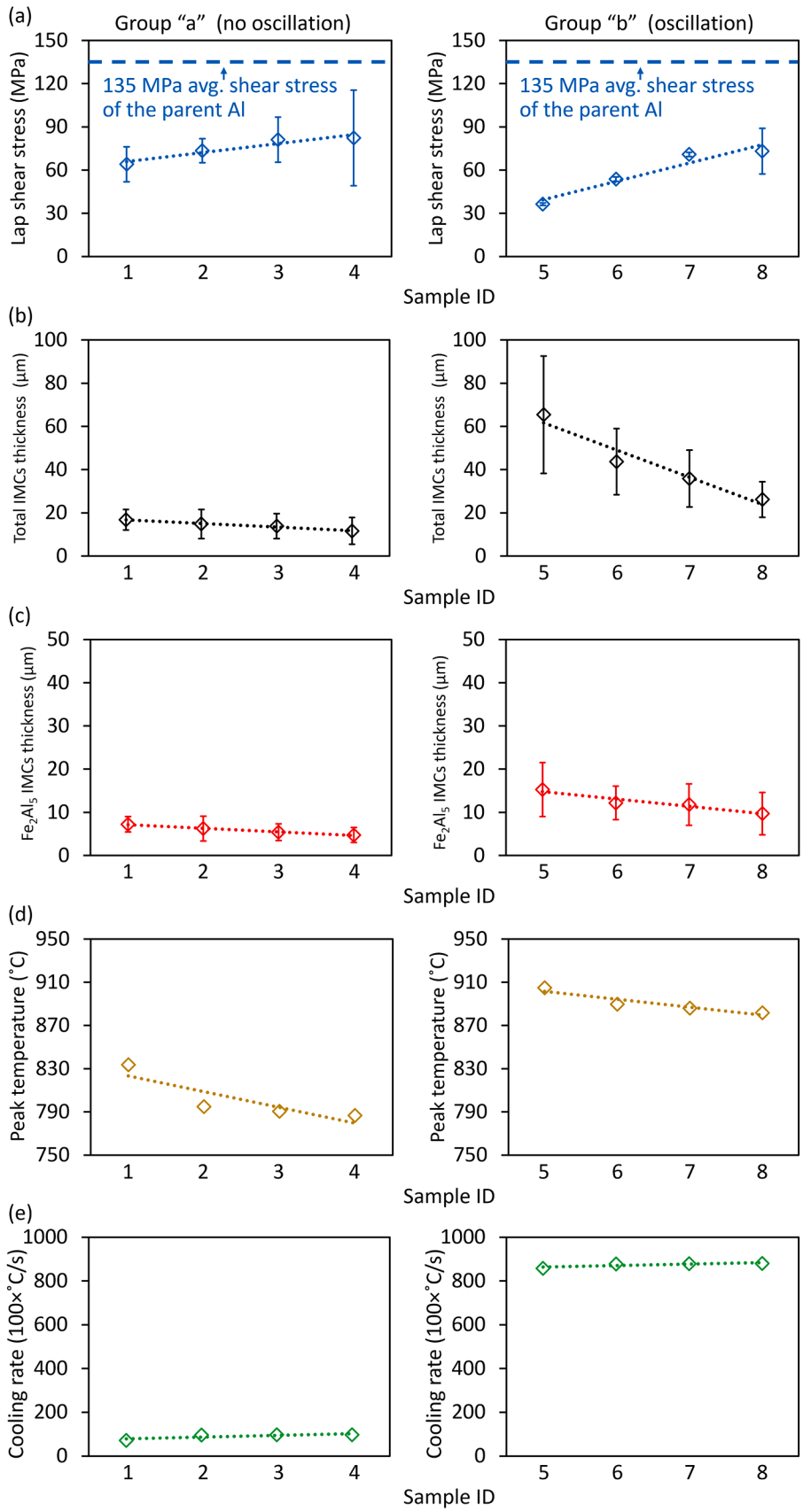

Fig. 9. Summary of the key determining factors for group "a" and group "b" at room temperature with no water flow (ID 1 & ID 5), and water flow at 25 °C (ID 2 & ID 6), 17 °C (ID 3 & ID 7) and 10 °C (ID 4 & ID 8).

considering IMCs and it probably highlights a positive role of higher connection area in stabilising the molten pool. This means that larger connection area is more capable in producing repeatable results and is consistent with the fact that larger connection area leads to more uniform stress distribution and less pronounced stress concentration. Besides, any variability in the weld quality has a more profound impact in samples of group "a" with a small connection area. It is worth noting that, the highest variation in shear stress can be found in the sample with the highest cooling rate in each group (ID 4 and ID 8). This higher variation of the strength with increasing the cooling rate is mainly due to the negative effect of cooling on Zn vaporisation. That is due to more Zn vaporisation and spattering associated with faster cooling, and the resulting lack of uniform joint and random-shaped connection area according to interface (aluminium) for ID 4 and ID 8 in Fig. 10. In fact, the dual effect of cooling on IMCs and Zn vaporisation is in its peak in the highest cooling rate; strength increases due to the reduction in IMCs thickness, while the repeatability of the strength decreases due to higher Zn vaporisation. Higher spattering with reduction in water flow temperature was witnessed by the number of trials required to change the cover glass of the laser as well. In fact, the laser system alarmed for the cover glass change after three trials when water flow temperature was 10 °C (ID 8), while it was alarmed after 15 trials when the water flow temperature was 17 °C (ID 7) and after 20 trials when the temperature was 25 °C (ID 6). When there was no active cooling, or the joint area was not large (group "a") this problem was less critical.

Effects on connection area

Analysing the interface (aluminium) images (Fig. 10) of both group "a" (no oscillation) and "b" (oscillation) reveals significant non-uniformities as water flow temperature decreases. This behaviour primarily attributed to the increased Zn vaporisation when the cooling temperature decreases and it is more obvious in samples of group "b" (oscillation) due to larger area. In samples of group "b", beam oscillation was introduced in combination with the copper backing block to enlarge the joint area and check the effect of larger joint area. Beam oscillation is supposed to help outgassing and enlarging the weld width by distributing the heat more evenly across a wider region (Ba et al., 2021; Thiel et al., 2012).

Fig. 11 depicts the values of connection area and welding depth in samples of group "a" (no oscillation) and "b" (oscillation), respectively. Application of beam oscillation has resulted in larger connection area and deeper welding penetration in group "b". Reduction of the connection area and welding depth occurs in samples with active cooling and water flow temperature decreases (from ID 1 to ID 4 and from ID 5 to ID 8 in Fig. 11). This is due to the fact that higher cooling rate causes faster solidification in the weld pool and as a result lower melting of the interface occurs on the aluminium. One interesting point that is

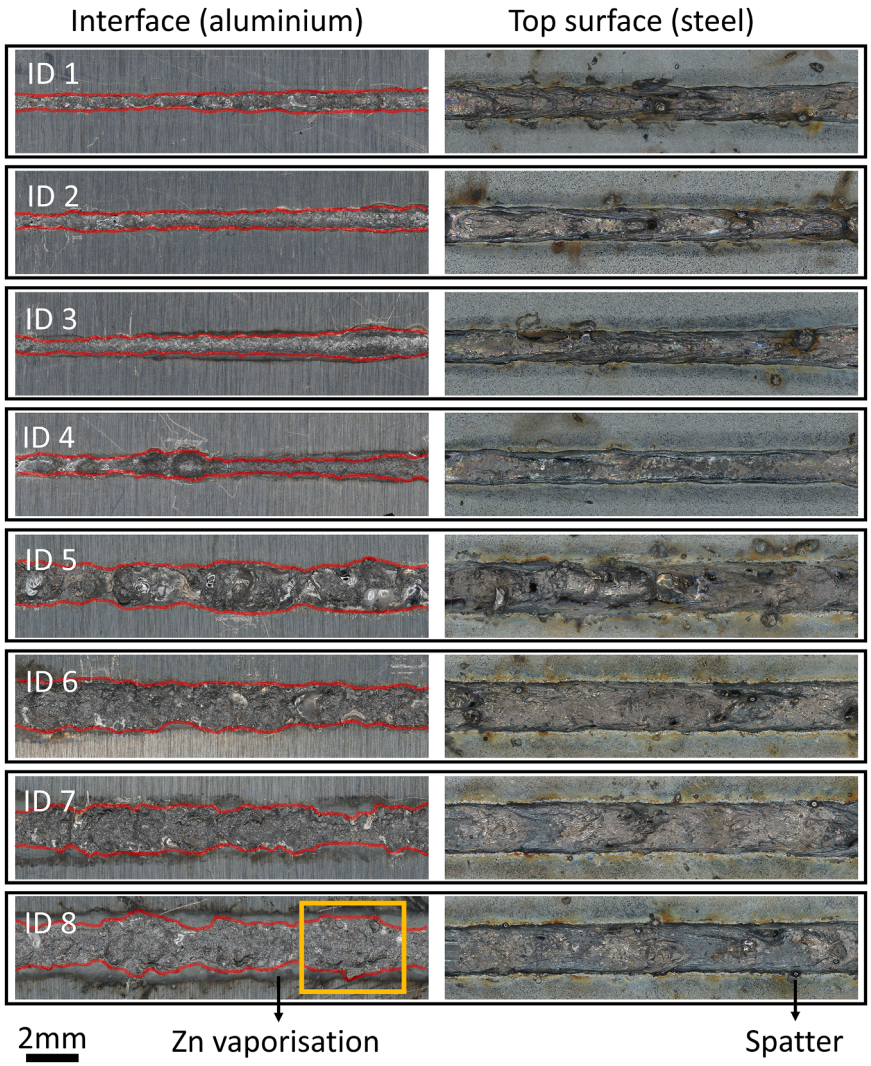

Fig. 10. Images of interface (aluminium) and top surface (steel) showing the features, including spattering and gas escape in various samples. The orange box in ID 8 interface (aluminium) specifies the region where EDS analysis in Fig. 8 were performed.

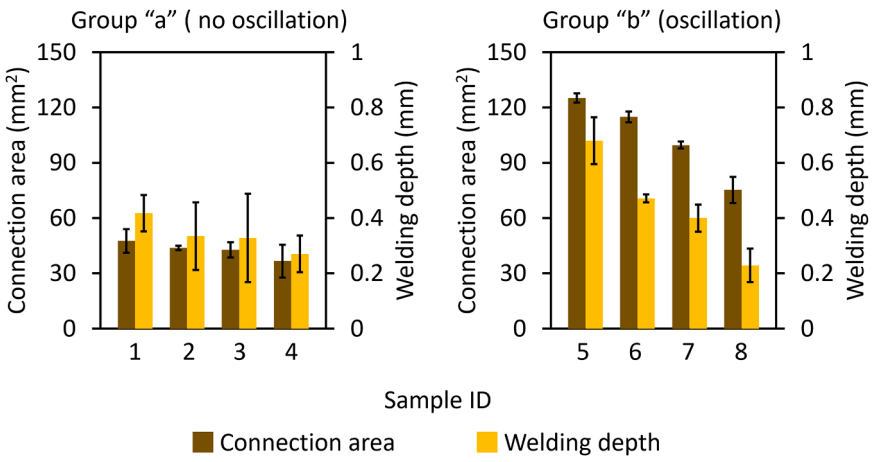

Fig. 11. Amount of connection area and welding depth for the samples welded in group “a” (no oscillation) and group “b” (oscillation).

observable in both groups is a large varation in connection area when water flow temperature is 10 °C (sample ID 4 and ID 8 in Fig. 11). This large variation in connection area is directly linked to the non uniform connection shape when temperature decreases to 10 °C. The negative impact of Zn vaporisation on reducing connection area and its uniformity has been reported in other works (Baghbani Barenji et al., 2024; Kapil et al., 2025). Considering the top surface (steel) in Fig. 10, one may consider no sign of increase in spattering as water temperature decrease despite more Zn gas mark in the interface (aluminium). It should be noted that when water flow is used and water temperature decreases, spattering intensifies, and spatter drops go to further distances rather than the specimen’s surface. This is the main reason for lack of spatter spectating on the top surface (steel) with decreasing the water flow temperature (from 25 °C in ID 2 and ID 6 to 10 °C in ID 4 and ID 8).

Impact of connection area and IMCs thickness on strength

Connection area, IMCs thickness and strength are interrelated properties that can be compared regardless of welding conditions such as cooling rate. Cooling influences both IMC thickness and connection area, making it impossible to isolate its effect on each factor individually. Similarly, since both IMCs thickness and connection area impact strength, identifying a trend for strength as a function of only IMC thickness or connection area is unfeasible. Nevertheless, general observations can suggest the influence of each factor. IMCs thickness is mainly affected by joint depth and width. Fig. 12 (a) and (b) illustrates changes in total IMCs thickness as a function of joint depth and joint width, respectively. While IMCs growth is simultaneously influenced by both welding depth and width, examining their effects separately in two diagrams provides valuable insights into the relative influence of each parameter. The slopes of the trendlines for total IMCs thickness as a function of joint depth and width are 0.113 and 0.027, respectively (Fig. 12). This indicates that joint depth has approximately four times more influence on IMC growth compared to joint width. This is understandable, considering that increased joint depth leads to greater mixing, resulting in faster IMCs growth. Additionally, this suggests that increasing joint width does not significantly increase IMCs thickness and can thus improve strength. The negative effect of excessively increasing the joint depth in dissimilar metals while welding in keyhole mode has been mentioned in literature (Jabar et al., 2023). This conclusion can explain that higher penetration in samples of group “b” (oscillation) resulted in higher amount of total and Fe_2Al_5 IMCs thickness. Regarding the strength, IMCs thickness and connection area are the primary factors affecting it. Fig. 13 demonstrates the changes in shear stress as a function of connection area, total IMCs and Fe_2Al_5 IMCs thickness. The data reveals high negative correlation between joint strength with connection area (-0.81), total IMC thickness (-0.90) and Fe_2Al_5 IMCs thickness (-0.85). This notable negative correlation elucidates that increasing the connection area does not improve the strength. This is primarily because the positive effect of enlarging the joint area is offset by the negative impact of IMCs when the connection area grows (and it is in contrast to the fact that an increase in connection area typically increases the bearable load). Also, as it was expected, increase in total and Fe_2Al_5 IMC thickness, declines strength due to more susceptibility to cracking. Thus, it can be concluded that a larger joint area cannot mitigate the adverse impact of increased IMC thickness and Zn vaporisation, although some improvements in shear stress and its variation can be seen by faster cooling in a moderate temperature (17 °C in ID 7). To further investigate the effects of cooling and joint area enlargement on the responses - such as joint strength, total IMCs thickness, Fe_2Al_5 thickness, connection area, and welding depth – a one-way ANOVA test was performed separately in each group of samples, with the results presented in Table 6. The test assessed whether the means of all samples within the setup were the same, against the alternative hypothesis that at least one mean differs. If the p-value exceeds 0.1, the null hypothesis is accepted. Table 6 indicates that the presence of cooling (group “a” (no oscillation)) and the

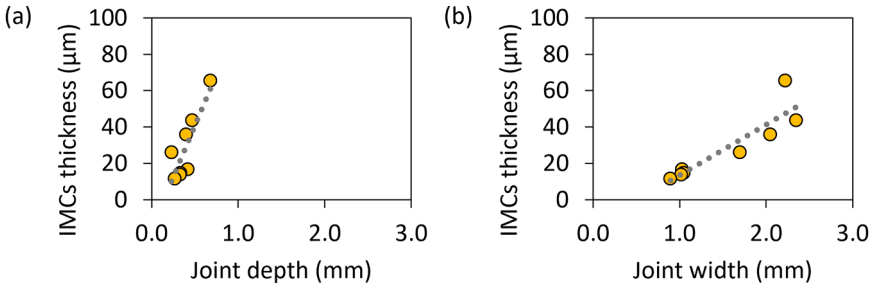

Fig. 12. The effect of (a) joint depth and (b) joint width on the increase of the IMCs thickness.

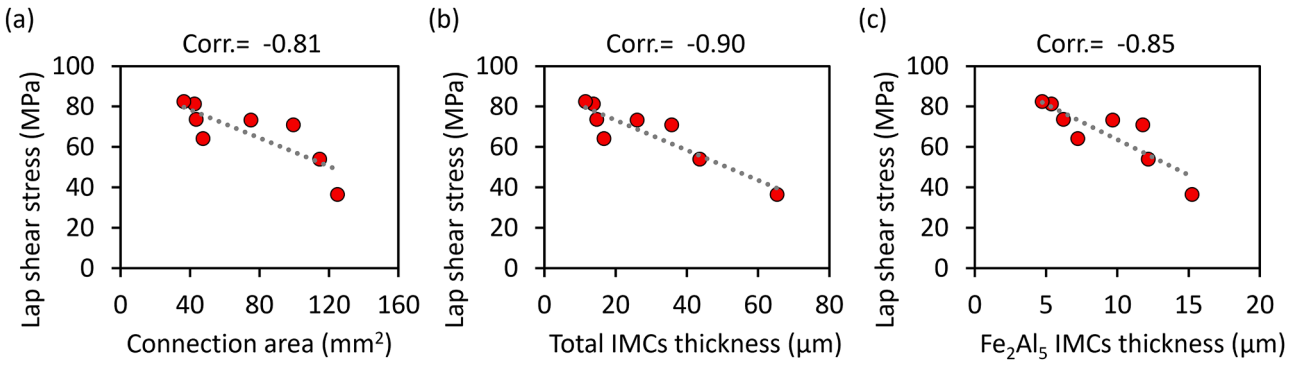

Fig. 13. The changes in linear load as a function of (a) connection area, (b) total IMCs thickness, and (c) Fe_2Al_5 IMCs thickness.

Table 6
Summary of the ANOVA tests with p-values (bold values represent statistical significance between factors).

Responses	Source Group "a" (cooling and no oscillation)	Source Group "b" (cooling and oscillation)
Shear stress	0.6654	**0.0016**
Total IMCs thickness	**0.0012**	**0**
Fe_2Al_5 IMCs thickness	**0.000003**	**0.00003**
Connection area	0.228	**0**
Welding depth	0.4855	**0.00009**

combination of cooling with beam oscillation to enlarge the joint area (group "b" (oscillation)) significantly affect the total IMCs thickness and Fe_2Al_5 thickness. However, shear stress, connection area and welding depth are not influenced by cooling alone (group "a" (no oscillation)), though they are affected by the combination of cooling and joint area enlargement (group "b" (oscillation)). Beam oscillation does enlarge the connection area and stabilise the molten pool. With beam oscillation, active cooling at 10 °C resulted in 74 MPa of shear strength, representing 54% of the strength of the parent aluminium and a 103% improvement compared to passive cooling (36 MPa). Without beam oscillation, passive cooling led to 64 MPa of shear strength, which is approximately double that of passive cooling with beam oscillation. On the other hand, active cooling at 10 °C yields 82 MPa shear strength, representing 60% of the strength of the parent aluminium and a 28% improvement over passive cooling. The sharper increase trend in strength with beam oscillation can be due to the faster reduction of IMCs thickness. Also, better repeatability of the strength was achieved in the samples with beam oscillation although spattering and Zn vaporisation is more intensive in these samples. This is attributed to the positive effect of larger connection area in mitigating the defects.

Conclusion

Laser welding of dissimilar hot-dip galvanised DC01 steel to 5251-H22 aluminium parts was conducted in a zero-gap overlap configuration and the effect of passive and active cooling on Zn vaporisation and IMCs growth were investigated. A 3D FEM thermal model was also used to link the thermal cycles to the experimental results. The key findings are summarised as follows:

- Increasing the cooling rate through active cooling has a positive effect in reducing IMCs thickness. Higher cooling rates reduce the peak temperature and diffusion time and as a result the growth of IMCs is limited. In group "a" (no oscillation), the cooling rate increased by 34% when switching from passive to active cooling. In contrast, in group "b" (with 2.5 mm lateral oscillation), the cooling rate increased by only 2.5% under the same change in cooling method. This resulted in a shear stress of 82 MPa, which corresponds to 60% of the joint efficiency compared to the parent aluminium.
- Fast cooling has dual effect in the welding process of a Zn-coated steel. On one hand, it reduces the IMCs thickness and provides high strength. On the other hand, fast cooling also increases the Zn vaporisation and spattering, which negatively affects the strength and the stability of the weld pool.
- Zn coating causes difficulties in welding Zn-coated steel to Al in overlap configuration as it evaporates during welding and causes spattering. Especially, when active cooling is applied, the disruptive influence of Zn vaporisation is seen by more spattering and non-uniform shape of the joint.
- Although beam oscillation increases the connection area and helps with stabilising the molten pool, does not lead to an improvement in shear stress compared to the scenario without oscillation. This is primarily due to higher formation of brittle IMCs, which have a greater negative impact than the beneficial effect of the larger connection area.

Future work will study the corrosion resistance properties of the welded samples, and will explore novel beam shaping (both static and dynamic) approaches to control the cooling rates via fast spatial and temporal modulation of the heat input. Additionally, the effect of a shielding gas system and a localised vapour extraction system on weld stability and efficiency will be analysed.

CRediT authorship contribution statement

A. Baghbani Barenji: Writing – review & editing, Writing – original draft, Formal analysis, Methodology, Investigation. **M.B. Russo:** Formal analysis, Methodology. **S. Jabar:** Formal analysis. **H.R. Kotadia:** Supervision, Writing – review & editing. **D. Ceglarek:** Supervision. **K.F. Ayarkwa:** Funding acquisition. **J.R. Smith:** Funding acquisition. **P. Franciosa:** Writing – review & editing, Supervision, Methodology, Funding acquisition.

Declaration of competing interest

The authors declare that they have no known competing financial interests or personal relationships that could have appeared to influence the work reported in this paper.

Acknowledgment

This work was supported by EPSRC JLR iCase voucher 20000095 (Remote Laser Welding of Dissimilar Metals for Automotive Structural Applications).

Data availability

The data that has been used is confidential.

References

Allen, T.R., Huang, W., Tanner, J.R., Tan, W., Fraser, J.M., Simonds, B.J., 2020. Energy-coupling mechanisms revealed through simultaneous keyhole depth and absorptance measurements during laser-metal processing. Phys. Rev. Appl. 13 (6), 064070. https://doi.org/10.1103/PHYSREVAPPLIED.13.064070/FIGURES/8/MEDIUM. Jun.

Artinov, A., Bachmann, M., Rethmeier, M., 2018. Equivalent heat source approach in a 3D transient heat transfer simulation of full-penetration high power laser beam welding of thick metal plates. Int. J. Heat. Mass Transf. 122, 1003–1013. https://doi.org/10.1016/J.IJHEATMASSTRANSFER.2018.02.058. Jul.

Ba, Y., et al., 2021. Microstructure and mechanical properties of laser oscillated welded DP780 dual phase steel and 5083 aluminium alloy: scanning oscillations at the same energy density. Lasers Eng. (Old City Publ.) 51, 299–313.

Baghbani Barenji, A., et al., 2024. Understanding the interplay of Zn vapours and formation of intermetallic compounds during remote laser welding of Zn-coated steel to aluminium in a zero-gap lap joint configuration. Procedia CIRP. 124, 678–683. https://doi.org/10.1016/J.PROCIR.2024.08.200. Jan.

Barnard, R.W., Pearce, K., Schovanec, L., 2001. Inequalities for the perimeter of an ellipse. J. Math. Anal. Appl. 260 (2), 295–306. https://doi.org/10.1006/jmaa.2000.7128.

Beygi, R., Galvão, I., Akhavan-Safar, A., Pouraliakbar, H., Fallah, V., da Silva, L.F.M., 2023. Effect of alloying elements on intermetallic formation during friction stir welding of dissimilar metals: a critical review on aluminum/steel. Metals. (Basel) 13 (4), 768. https://doi.org/10.3390/MET13040768. *2023, Vol. 13, Page 768*Apr.

Borrisutthekul, R., Yachi, T., Miyashita, Y., Mutoh, Y., 2007. Suppression of intermetallic reaction layer formation by controlling heat flow in dissimilar joining of steel and aluminum alloy. Mater. Sci. Eng. A 467 (1–2), 108–113. https://doi.org/10.1016/j.msea.2007.03.049. Oct.

Bouayad, A., Gerometta, C., Belkebir, A., Ambari, A., 2003. Kinetic interactions between solid iron and molten aluminium. Mater. Sci. Eng. A 363 (1–2), 53–61. https://doi.org/10.1016/S0921-5093(03)00469-6. Dec.

Casalino, G., Leo, P., Mortello, M., Perulli, P., Varone, A., 2017. Effects of laser offset and hybrid welding on microstructure and IMC in Fe–Al dissimilar welding. Metals. (Basel) 7 (8), 282. https://doi.org/10.3390/MET7080282. *2017, Vol. 7, Page 282*Jul.

H.-C. Chen, A.J. Pinkerton, L. Li, Z. Liu, and A.T. Mistry, "Gap-free fibre laser welding of Zn-coated steel on Al alloy for light-weight automotive applications," 2010, doi: 10.1016/j.matdes.2010.08.034.

Chludzinski, M., Dos Santos, R.E., Churiaque, C., Sánchez-Amaya, J.M., Ortega-Iguña, M., 2021. Pulsed laser welding applied to metallic materials—a material approach. Metals 11 (4), 640. https://doi.org/10.3390/MET11040640. *2021, Vol. 11, Page 640*Apr.

Dasgupta, A.K., Mazumder, ; J, Li, ; P, Mazumder, J., Li, P., 2007. Physics of zinc vaporization and plasma absorption during CO 2 laser welding. J. Appl. Phys. 102, 53108. https://doi.org/10.1063/1.2777132.

Daurelio, G., Dell'Erba, M., Cento, L., 1986. Cutting Copper Sheets by CO2 Laser (Long Thought Uncuttable on a Practical Basis, Copper Has Surrendered to the CO2 Laser). Lasers & Applications 5, 59–64.

Dourado da Silva, R.G., dos Santos Magalhães, E., de Lima e Silva, S.M.M., dos Santos Paes, L.E., Pereira, M., 2023. Estimating the absorption efficiency in a laser welding process using a nonlinear inverse problem method. Int. J. Thermal Sci. 183, 107846. https://doi.org/10.1016/J.IJTHERMALSCI.2022.107846. Jan.

EN ISO, 2000. 14273. Specimen Dimensions and Procedure for Shear Testing Resistance Spot, Seam and Embossed Projection Welds, 2. International Organization for Standardization, Geneva, Switzerland.

GRYC, K., SMETANA, B., STROUHALOVÁ, M., ŽALUDOVÁ, M., MICHALEK, K., ZLÁ, S., VÁLEK, L., KALUP, A., & DOBROVSKÁ, J., Determination of solidus and liquidus temperatures in the low carbon steel using three devices for high-temperature thermal analysis and specialized programs. METHODOLOGY, 14, 15..

Guo, Q., et al., 2019. In-situ characterization and quantification of melt pool variation under constant input energy density in laser powder bed fusion additive manufacturing process. Addit. Manuf. 28, 600–609. https://doi.org/10.1016/J.ADDMA.2019.04.021. Aug.

Hao, Y., Wang, H.P., Sun, Y., Li, L., Wu, Y., Lu, F., 2022. The evaporation behavior of zinc and its effect on spattering in laser overlap welding of galvanized steels. J. Mater. Process. Technol. 306, 117625. https://doi.org/10.1016/J.JMATPROTEC.2022.117625. Aug.

Hertwich, E.G., et al., 2019. Material efficiency strategies to reducing greenhouse gas emissions associated with buildings, vehicles, and electronics - a review. Environ. Res. Lett. 14 (4). https://doi.org/10.1088/1748-9326/ab0fe3. Apr.

Jabar, S., et al., 2023. Effect of a ring-shaped laser beam on the weldability of aluminum-to-hilumin for battery tab connectors. J. Laser Appl. 35 (4). https://doi.org/10.2351/7.0001156/2916232. Nov.

Jabar, S., Baghbani Barenji, A., Franciosa, P., Kotadia, H.R., Ceglarek, D., 2023. Effects of the adjustable ring-mode laser on intermetallic formation and mechanical properties of steel to aluminium laser welded lap joints. Mater. Design 227, 111774. https://doi.org/10.1016/j.matdes.2023.111774.

Kapil, A., Vivek, A., Daehn, G., 2025. Role of zinc coating on joint properties in impact spot welded Al 6111 aluminum alloy to galvanized high-strength low-alloy steel. J. Adv. Join. Process. 11, 100276. https://doi.org/10.1016/j.jajp.2024.100276.

Karim, Md.A., Park, Y.-D., 2020. A review on welding of dissimilar metals in car body manufacturing. J. Weld. Join. 38 (1), 8–23. https://doi.org/10.5781/JWJ.2020.38.1.1. Feb.

Kashani, H.T., Kah, P., Martikainen, J., 2015. Laser overlap welding of zinc-coated steel on aluminum alloy. Phys. Procedia 78, 265–271. https://doi.org/10.1016/j.phpro.2015.11.037.

Kotadia, H.R., Franciosa, P., Jabar, S., Ceglarek, D., 2022. Remote laser welding of Zn coated IF steel and 1050 aluminium alloy: processing, microstructure and mechanical properties. J. Mater. Res. Technol. 19, 449–465. https://doi.org/10.1016/J.JMRT.2022.05.041. Jul.

Kuryntsev, S., 2021. A review: laser welding of dissimilar materials (Al/Fe, Al/Ti, Al/Cu)—methods and techniques, microstructure and properties. Materials 15 (1), 122. https://doi.org/10.3390/MA15010122. *2022, Vol. 15, Page 122*Dec.

Li, Y., Liu, Y., Yang, J., 2020. First principle calculations and mechanical properties of the intermetallic compounds in a laser welded steel/aluminum joint. Opt. Laser. Technol. 122, 105875. https://doi.org/10.1016/J.OPTLASTEC.2019.105875. Feb.

Liedl, G., et al., 2011. Joining of aluminum and steel in car body manufacturing. Phys. Procedia 12 (PART 1), 150–156. https://doi.org/10.1016/J.PHPRO.2011.03.019. Jan.

Liu, Y.H., Chong, X.Y., Jiang, Y.H., Zhou, R., Feng, J., 2017. Mechanical properties and electronic structures of Fe-Al intermetallic. Phys. B Condens. Matter 506, 1–11. https://doi.org/10.1016/J.PHYSB.2016.10.032. Feb.

J. Ma, M. Harooni, B. Carlson, and R. Kovacevic, "Dissimilar joining of galvanized high-strength steel to aluminum alloy in a zero-gap lap joint configuration by two-pass laser welding," 2014, doi: 10.1016/j.matdes.2014.01.046.

Ma, B., Gao, X., Huang, Y., Gao, P.P., Zhang, Y., 2023. A review of laser welding for aluminium and copper dissimilar metals. Opt. Laser. Technol. 167, 109721. https://doi.org/10.1016/J.OPTLASTEC.2023.109721. Dec.

"Overview of materials for 5000 series aluminum alloy." Accessed: Nov. 04, 2024.https://www.matweb.com/search/datasheet_print.aspx?matguid=c71186d128cd423d9c6d51106c015e8f.

Meng, Y., Gong, M., Zhang, S., Zhang, Y., Gao, M., 2020. Effects of oscillating laser offset on microstructure and properties of dissimilar Al/steel butt-joint. Opt. Lasers. Eng. 128, 106037. https://doi.org/10.1016/J.OPTLASENG.2020.106037. May.

Ozaki, H., Kutsuna, M., 2012. Dissimilar metal joining of zinc coated steel and aluminum alloy by laser roll welding. Weld. Process. 2 (2), 33–54.

Ozkat, E.C., Franciosa, P., Ceglarek, D., 2017. Laser dimpling process parameters selection and optimization using surrogate-driven process capability space. Opt. Laser. Technol. 93, 149–164. https://doi.org/10.1016/J.OPTLASTEC.2017.02.012. Aug.

Pardal, G., Meco, S., Ganguly, S., Williams, S., Prangnell, P., 2014. Dissimilar metal laser spot joining of steel to aluminium in conduction mode. Int. J. Adv. Manuf. Technol. 73 (1–4), 365–373. https://doi.org/10.1007/s00170-014-5802-y.

Quazi, M.M., et al., 2020. Current research and development status of dissimilar materials laser welding of titanium and its alloys. Opt. Laser. Technol. 126, 106090. https://doi.org/10.1016/J.OPTLASTEC.2020.106090. Jun.

Sadeghian, A., Iqbal, N., 2022. A review on dissimilar laser welding of steel-copper, steel-aluminum, aluminum-copper, and steel-nickel for electric vehicle battery manufacturing. Opt. Laser. Technol. 146, 107595. https://doi.org/10.1016/J.OPTLASTEC.2021.107595. Feb.

L.H. Shah and M. Ishak, "Review of research progress on aluminum–steel dissimilar welding," *10.1080/10426914.2014.880461*, vol. 29, no. 8, pp. 928–933, Aug. 2014, doi: 10.1080/10426914.2014.880461.

Shang, S.L., et al., 2021. Forming mechanism of equilibrium and non-equilibrium metallurgical phases in dissimilar aluminum/steel (Al–Fe) joints. Sci. Rep. 11 (1), 1–15. https://doi.org/10.1038/s41598-021-03578-0. *2021 11:1*Dec.

Simonds, B.J., et al., 2018. Dynamic and absolute measurements of laser coupling efficiency during laser spot welds. Procedia CIRP 74, 632–635. https://doi.org/10.1016/J.PROCIR.2018.08.065. Jan.

Singh, J., Arora, K.S., Shukla, D.K., 2019. Dissimilar MIG-CMT weld-brazing of aluminium to steel: a review. J. Alloys Compd. 783, 753–764. https://doi.org/10.1016/J.JALLCOM.2018.12.336. Apr.

Sun, T., Franciosa, P., Ceglarek, D., 2021. Effect of focal position offset on joint integrity of AA1050 battery busbar assembly during remote laser welding. J. Mater. Res. Technol. 14, 2715–2726. https://doi.org/10.1016/J.JMRT.2021.08.002. Sep.

C. Thiel, A. Hess, R. Weber, and T. Graf, "Stabilization of laser welding processes by means of beam oscillation," *10.1117/12.922403*, vol. 8433, pp. 225–234, May 2012, doi: 10.1117/12.922403.

D. Wallerstein et al., "Recent developments in laser welding of aluminum alloys to steel," 2021, doi: 10.3390/met11040622.

Xia, H., Zhang, L., Tan, C., Wu, L., Chen, B., Li, L., 2019. Effect of heat input on a laser powder deposited Al/steel butt joint. Opt. Laser. Technol. 111, 459–469. https://doi.org/10.1016/J.OPTLASTEC.2018.10.032. Apr.

Xie, L., et al., 2022. Effect of dynamic preheating on the thermal behavior and mechanical properties of laser-welded joints. Materials 15 (17), 6159. https://doi.org/10.3390/MA15176159. *2022, Vol. 15, Page 6159*Sep.

Xu, L., Wang, L., Chen, Y.C., Robson, J.D., Prangnell, P.B., 2016. Effect of interfacial reaction on the mechanical performance of steel to aluminum dissimilar ultrasonic spot welds. Metall. Mater. Trans. A Phys. Metall. Mater. Sci. 47 (1), 334–346. https://doi.org/10.1007/S11661-015-3179-7/FIGURES/11. Jan.

Yang, Y., Luo, Z., Zhang, Y., Su, J., 2024. Dissimilar Welding of Aluminium to Steel: A Review. Elsevier Ltd. https://doi.org/10.1016/j.jmapro.2023.12.060. Jan. 31.

Zarei, A., Akbari, M., Abdollahi, A., Soleimanimehr, H., 2024. Experimental and numerical study of dissimilar fiber laser welding of martensitic AISI 1060 carbon steel with different configuration with austenitic 304 and ferritic 420 stainless steel. Heliyon 10 (21), e39954. https://doi.org/10.1016/J.HELIYON.2024.E39954. Nov.

Zhang, Y., Zhao, T., Yu, X., Huang, J., 2023. The Al-Fe intermetallic compounds and the atomic diffusion behavior at the interface of aluminum-steel welded joint. Metals. (Basel) 13 (2), 334. https://doi.org/10.3390/MET13020334. *2023, Vol. 13, Page 334*Feb.